Episodically Active Asteroid 6478 Gault

David Jewitt[1,2], Yoonyoung Kim[3], Jane Luu[4], Jayadev Rajagopal[5], Ralf Kotulla[6], Susan Ridgway[5], and Wilson Liu[5]

[1] Department of Earth, Planetary and Space Sciences, UCLA, 595 Charles Young Drive East, Los Angeles, CA 90095-1567, USA; jewitt@ucla.edu
[2] Dept. of Physics and Astronomy, UCLA, 430 Portola Plaza, Box 951547, Los Angeles, CA 90095-1547, USA
[3] Max Planck Institute for Solar System Research, Justus-von-Liebig-Weg 3, D-37077 Göttingen, Germany
[4] Department of Physics and Technology, Arctic University of Tromso, Tromso, Norway
[5] NOAO, 950 North Cherry Avenue, Tucson, AZ 85719, USA
[6] Department of Astronomy, University of Wisconsin-Madison, 475 N. Charter St., Madison, WI 53706, USA

Received 2019 April 10; revised 2019 April 23; accepted 2019 April 24; published 2019 May 6

Abstract

We present imaging and spectroscopic observations of 6478 Gault, a $\sim$6 km diameter inner main-belt asteroid currently exhibiting strong, comet-like characteristics. Three distinct tails indicate that ultra-slow dust (ejection speed $0.15 \pm 0.05 \, \mathrm{m \, s^{-1}}$) was emitted from Gault in separate episodes beginning UT 2018 October 28 $\pm$ 5 (Tail A), UT 2018 December 31 $\pm$ 5 (Tail B), and UT 2019 February 10 $\pm$ 7 (Tail C), with durations of $\Delta T \sim$ 10–20 days. With a mean particle radius $\overline{a} \sim 200 \, \mu m$, the estimated masses of the tails are $M_A \sim 4 \times 10^7 \, \mathrm{kg}$, $M_B \sim 6 \times 10^6 \, \mathrm{kg}$, and $M_C \sim 6 \times 10^5 \, \mathrm{kg}$, respectively, and the mass-loss rates from the nucleus are 20–40 kg s^{-1} for Tail A, 4–6 kg s^{-1} for Tail B, and $\sim$0.4 kg s^{-1} for Tail C. In its optical colors Gault is more similar to C-type asteroids than to S-types, even though the latter are numerically dominant in the inner asteroid belt. A spectroscopic upper limit to the production of gas is set at 1 kg s^{-1}. Discrete emission in three protracted episodes effectively rules out an impact origin for the observed activity. Sublimation driven activity is unlikely given the inner-belt orbit and the absence of detectable gas. In any case, sublimation would not easily account for the observed multiple ejections. The closest similarity is between Gault and active asteroid 311P/(2013 P5), an object showing repeated but aperiodic ejections of dust over a 9 month period. While Gault is 10 times larger than 311P/(2013 P5), and the relevant timescale for spin-up by radiation torques is $\sim$100 times longer, its properties are likewise most consistent with episodic emission from a body rotating near breakup.

Key words: comets: general – minor planets, asteroids: general – minor planets, asteroids: individual (6478 Gault)

1. Introduction

Main-belt asteroid 6478 Gault (formerly 1988 JC1 and simply "Gault," hereafter) was first reported to be active in observations from the Asteroid Terrestrial-impact Last Alert System (ATLAS) telescope on UT 2019 January 8, when it sported a long, thin tail (Smith et al. 2019). Soon, archival observations from the Zwicky Transient Facility (ZTF) survey emerged to show dust emission from Gault starting as early as 2018 October, with peaks in the brightness near UT 2018 October 31 and UT 2018 December 30 (Ye et al. 2019). The orbital elements (semimajor axis $a = 2.305$ au, eccentricity $e = 0.194$, and inclination $i = 22°.8$), qualify Gault as a member of the Phocaea asteroid group, the latter being bounded by $2.1 < a < 2.5$ au, $0.0 < e < 0.4$, and $17° < i < 30°$ (Novaković et al. 2017). If substantiated, this association may suggest that Gault is a fragment from a 260 ± 40 Myr old shattering collision. The inner-belt orbit of Gault is near to active asteroids 354P/(2010 A2) and 311P/(2013 P5). Of these, the former is a product of hypervelocity impact onto a $\sim$100 m scale primary (Jewitt et al. 2010, 2013b; Kim et al. 2017a, 2017b). The cause of episodic mass loss in the latter is less clear, but likely reflects incipient rotational instability (Jewitt et al. 2013a, 2015; Hainaut et al. 2014; Hirabayashi et al. 2015); 311P may also be an eclipsing binary (Jewitt et al. 2018). Several active asteroids in the outer belt have been associated with repeated episodes of near-perihelion mass loss, leading to the suggestion that they are driven by the sublimation of near-surface water ice (Hsieh & Jewitt 2006). The diversity of origins of the activity in otherwise dynamically unremarkable asteroids leads to the inevitable question: what drives the activity in Gault?

In this Letter, we present imaging and spectroscopic observations taken to characterize the ongoing mass loss from this formerly unremarkable asteroid.

2. Observations

2.1. Imaging

We used the 2.56 m diameter Nordic Optical Telescope (NOT), located on La Palma, the Canary Islands, and the Andalucia Faint Object Spectrograph and Camera (ALFOSC) optical camera. ALFOSC is equipped with a 2048×2064 pixel "e2v Technologies" charge-coupled device, giving an image scale of $0''.214$ pixel^{-1}, and a vignette-limited field of view approximately $6'.5 \times 6'.5$. Broadband Bessel B (central wavelength $\lambda_c = 4400$ Å, FWHM $\Delta \lambda = 1000$ Å), V ($\lambda_c = 5300$ Å, $\Delta \lambda = 800$ Å), and R ($\lambda_c = 6500$ Å, $\Delta \lambda = 1300$ Å) filters were used. The NOT was tracked at non-sidereal rates to follow Gault, while autoguiding using field stars. We obtained a series of images each of 70 s integration during which time field objects trailed by $\sim$0''.01 on UT 2019 January 10 but by $\sim$0''.9 on UT 2019 February 21 and $\sim$0''.6 on UT 2019 April 10. The images were first bias subtracted and then normalized by a flat-field image constructed from images of the illuminated interior of the observatory dome. Photometric calibration of the data was obtained by reference to standard star PG 0918 + 029A (Landolt 1992). Measurements of field stars show that the atmosphere was photometric to $\lesssim$0.01 mag. The field stars were also used to measure the extinction, found to be 0.18,

0.12, and 0.06 mag per airmass in the *B, V,* and *R* filters, respectively. Seeing was variable in the range 1″0 FWHM to 1″3 FWHM. NOT data from UT 2019 February 21 suffered from strong internal scattering due to moonlight, but this was largely removed in the processing of the data.

Additional observations were taken on UT 2019 March 4 at the 3.5 m diameter WIYN telescope, located at Kitt Peak National Observatory in Arizona (see Table 1). We used the One Degree Imager camera mounted at the Nasmyth focus with a rebinned image scale of 0.25 pixel^{-1} (Harbeck et al. 2014). Observations were taken through the Sloan *r′* (central wavelength $\lambda_c = 6250$ Å, FWHM = 1400 Å) filter with an accumulated integration of 6300 s (180 s individual integration time). Median seeing was 1″1 FWHM. For data reduction we used the "Quickreduce" pipeline (Kotulla 2014), and photometric calibration of the data was made with reference to the Sloan DR 14 database (Blanton et al. 2017).

We also used publicly accessible observations from the *Hubble Space Telescope* (*HST*; GO 15678, PI: Meech) taken on UT 2019 February 5. These consist of five images per visit, with 380 s exposures acquired through the F350 LP broadband filter (central wavelength 6230 Å, FWHM = 4758 Å) using the WFC3 camera. The pixel size was 0″04 pixel^{-1}. The images were shifted to a common center and median combined to eliminate cosmic rays to produce a composite image that was used for all measurements. Unfortunately, the nucleus of Gault is saturated in the *HST* data, which therefore cannot be used to study the near-nucleus environment at high resolution. Here, we use the *HST* composites only to measure the tail position angles (PAs), as recorded in Table 1.

2.2. Photometry and Light Curve

A composite image from UT 2019 January 10, formed by shifting the *R*-band images of combined exposure time 6790 s to a common center, is shown in Figure 1. The asteroid shows a single, prominent tail ("Tail A") at position angle PA = 291°0 ± 0°5 that is aligned with neither the antisolar direction nor the projected negative heliocentric velocity vector. A single image taken in the process of recording a spectrum on UT 2019 January 20 (see Section 2.4) showed this same tail (PA = 292° ± 1°) plus a second, stubby tail at PA = 301° ± 1°. This second, stubby tail ("Tail B") is better recorded in NOT images from UT 2019 February 21 (Figure 2) and WIYN on UT 2019 March 3 (Figure 3). These later images show that the second tail is shorter and brighter than the first, resulting from more recent ejection of dust. By UT 2019 March 24 (Figure 4), when the Earth passed through the projected orbital plane of Gault, Tails A and B were merged. Observations on UT 2019 April 10 from $\delta_E = -4°$ below the plane show Tails A and B widely splayed, and the emergence of new Tail C (Figure 5).

We searched for evidence of dust between Tails A and B by making plots of the surface brightness perpendicular to the midline between the tails, using the high signal-to-noise ratio image from UT 2019 March 3 (Figure 3). The search is compromised by ultra-faint field galaxies whose trails are aligned roughly parallel to the tail midline, and no Gault-associated dust could be detected.

Time-series measurements of the apparent magnitude of the near-nucleus region, m_V, were obtained from UT 2019 January 10, the data with the longest timebase. We used circular apertures with angular radii 10, 15, and 20 pixels (2″1, 3″2 and

4″3, respectively), with sky subtraction from a contiguous annulus having an outer radius 8″4. Calibration against field and Landolt stars was made using the same apertures. We used measurements of nearby field stars, obtained with the same photometric apertures, to assess variable atmospheric extinction as the airmass varied in the range 1.3–1.8 over the 3 hr of observation.

In Figure 6 we show a sample photometric time-series measured at ∼2 minute cadence on UT 2019 January 10. In a phase dispersion minimization analysis of the data, we find no evidence for cyclic (rotational) brightness variation at the ∼1% level or larger. The same invariance of the photometry is observed using the 2″1 and 3″1 apertures. This is in agreement with the findings of Moreno et al. (2019) and Ye et al. (2019). Kleyna et al. (2019) report evidence for a ∼1 hr periodogram peak in longer time-series from several telescopes. However, they find no convincing light curve, perhaps because of the influence of systematic uncertainties in the data, and/or weak and transient activity. The lack of a measurable light curve is consistent with Gault having a shape that is close to azimuthally symmetric, or a rotation vector parallel to the line of sight, or with the scattering cross section being dominated by dust.

To address this latter possibility, we computed the absolute magnitude from our data to compare with the absolute magnitude recorded in the JPL Horizons online database. The apparent magnitudes, m_V, and absolute magnitudes, H, are related by the inverse square law

$$H = m_V - 2.5\log_{10}(r_H^2\Delta^2) + 2.5\log_{10}(\Phi(\alpha)) \qquad (1)$$

where r_H and Δ are the heliocentric and geocentric distances expressed in astronomical unit and $\Phi(\alpha) \leqslant 1$ is the phase function measured at phase angle α. Equation (1) defines the absolute magnitude, H, as the magnitude the comet would have if it could be observed from $r_H = \Delta = 1$ au and $\alpha = 0°$. The relevant phase function for Gault is uncertain. For simplicity, we assume $2.5\log_{10}(\Phi(\alpha)) = -0.04\alpha$.

We further relate the absolute magnitudes to the effective scattering cross sections, C_e, by

$$C_e = \frac{1.5 \times 10^6}{p_V}10^{-0.4H} \qquad (2)$$

where p_V is the geometric albedo. The effective albedo of Gault, consisting of a mixture of light scattered from the nucleus and light scattered from dust, is uncertain. We here assume a nominal albedo $p_V = 0.1$, while acknowledging that the true value may be larger or smaller by a factor of several.

The catalog value of the absolute magnitude of Gault is $H = 14.4$ (JPL Horizons software). This is close to the absolute magnitude in NOT data from UT 2019 February 21, but 0.7 mag fainter than H determined on UT 2019 January 10 (Table 2). Through Equation (2), this difference corresponds to ∼20 km^2 excess in the near-nucleus cross section on January 10. This estimate is uncertain, however, by an amount that depends on the unknown phase function (and also on the unknown accuracy of the catalog absolute magnitude).

The apparent magnitudes and effective cross sections of dust tails A and B are best measured in the high signal-to-noise data from UT 2019 March 3 (Table 1). We again rotated the composite image to bring each tail to the horizontal, then measured the signal within projected rectangular boxes aligned

Table 1
Observing Geometry

UT Date	UT	Tel[a]	Mode[b]	DOY[c]	ν[d]	r_H[e]	Δ[f]	α[g]	$\theta_{-\odot}$[h]	θ_{-V}[i]	δ_E[j]	PA_A[k]	PA_B[k]	PA_C[k]
2019 Jan 10	02:04–05:12	NOT	BVR	10	238.8	2.466	1.833	20.4	304.4	269.8	11.6	291.0 ± 0.5	⋯	⋯
2019 Jan 20	02:11–02:53	NOT	Sp	20	241.3	2.446	1.713	18.4	309.2	270.3	11.6	292.0 ± 1.0	301.0 ± 1.0	⋯
2019 Feb 05	15:08–15:45	*HST*	F350LP	36	245.2	2.413	1.537	13.4	322.0	271.5	10.6	294.0 ± 0.5	306.0 ± 0.5	⋯
2019 Feb 21	00:27–01:44	NOT	BVR	52	249.3	2.382	1.429	8.2	350.5	272.5	8.2	293.5 ± 0.5	309.6 ± 0.7	⋯
2019 Feb 27	16:17–16:51	*HST*	F350LP	58	250.9	2.368	1.402	6.9	15.4	272.7	6.7	292.9 ± 0.5	311.2 ± 0.5	⋯
2019 Mar 03	04:43–07:17	WIYN	r′	62	252.2	2.360	1.392	6.7	31.7	272.7	5.9	291.1 ± 0.5	312.5 ± 0.5	⋯
2019 Mar 22	10:53–11:29	*HST*	F350LP	81	257.1	2.319	1.401	12.4	88.4	271.5	0.70	275.0 ± 0.5	298 ± 2	⋯
2019 Mar 24	00:16–01:21	NOT	R	83	257.6	2.315	1.406	13.0	90.3	271.3	0.26	271.6 ± 0.2	⋯	⋯
2019 Apr 9–10	23:31–00:36	NOT	R	100	262.3	2.278	1.495	19.5	103.0	268.9	−4.0	239 ± 1	151 ± 1	116 ± 1

Notes.
[a] NOT = NOT 2.5 m, *HST* = *Hubble Space Telescope* 2.6 m, WIYN = 3.5 m.
[b] BVR = imaging at 0″214 pixel^{-1}, Sp = spectrum, F350LP; see the text.
[c] Day of year number, 1 = UT 2019 January 1.
[d] True anomaly, in degrees.
[e] Heliocentric distance, in astronomical unit.
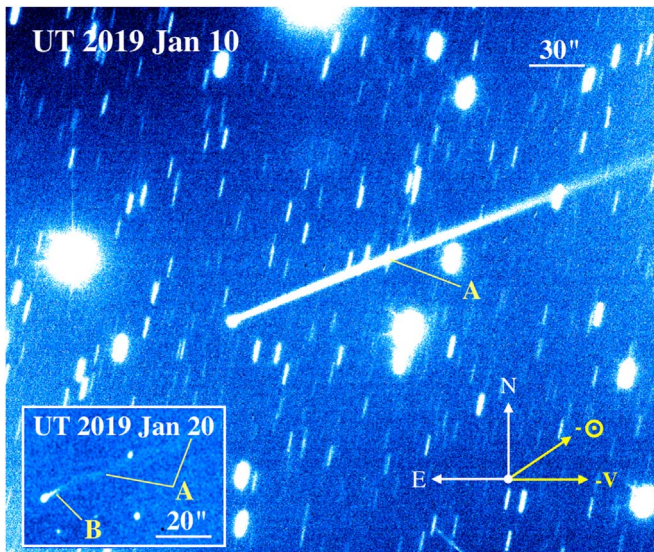[f] Geocentric distance, in astronomical unit.
[g] Phase angle, in degrees.
[h] Position angle of projected antisolar direction, in degrees.
[i] Position angle of negative projected orbit vector, in degrees.
[j] Angle of Earth above orbital plane, in degrees.
[k] Position angles of Tails A, B, and C.

Figure 1. Tail A of 6478 Gault on UT 2019 January 10, produced by combining 97 separate 70 s integrations (total exposure time 6790 s) with the NOT. Cardinal directions, a scale bar, and the antisolar and negative velocity vectors are shown. The inset shows Gault on UT 2019 January 20, when new Tail B (angled slightly more steeply than the main Tail A) is first visible.
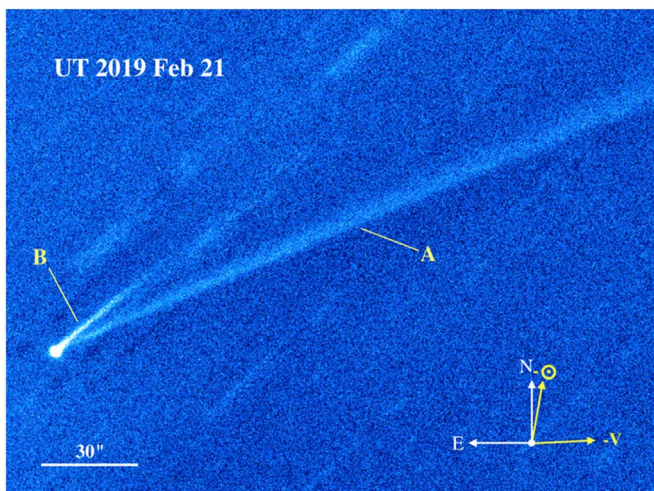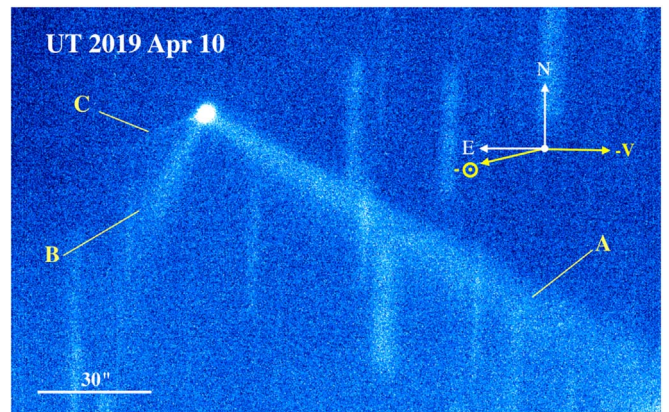

Figure 2. 6478 Gault on UT 2019 February 21, produced by combining 36 separate 70 s integrations (total exposure time 2520 s) with the NOT. Cardinal directions, a scale bar, and the antisolar and negative velocity vectors are shown. Background star and galaxy trail residuals are apparent.
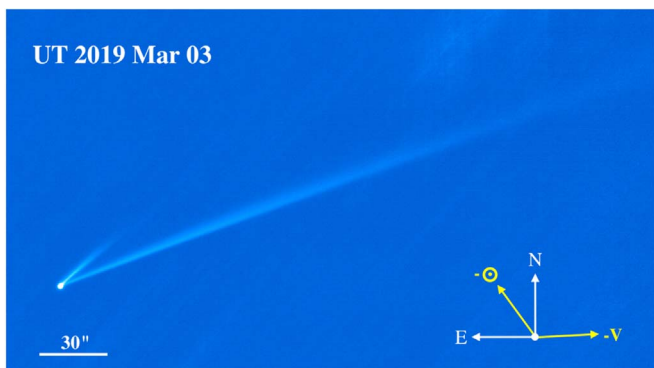

Figure 3. 6478 Gault on UT 2019 March 3, produced by combining 35 separate 180 s integrations (total exposure time 6300 s) from the WIYN telescope. Cardinal directions, a scale bar, and the antisolar and negative velocity vectors are shown.
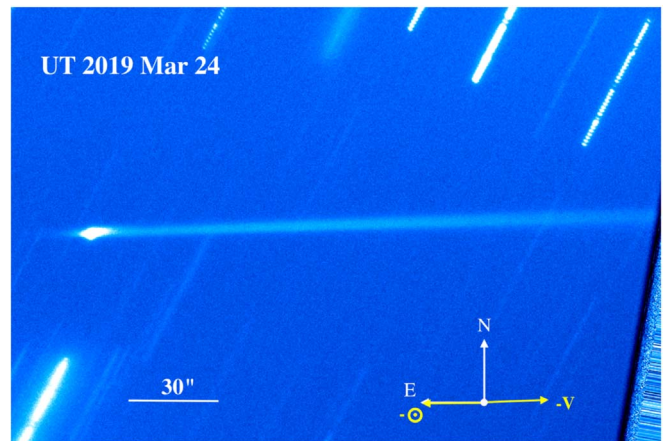
Figure 4. 6478 Gault on UT 2019 March 24, produced by combining 37 separate 60 s integrations (total exposure time 2220 s) from the NOT telescope. Cardinal directions, a scale bar, and the antisolar and negative velocity vectors are shown.

Figure 5. 6478 Gault on UT 2019 April 10, produced by combining 30 separate 60 s integrations (total exposure time 1800 s) from the NOT telescope. Cardinal directions, a scale bar, and the antisolar and negative velocity vectors are shown.
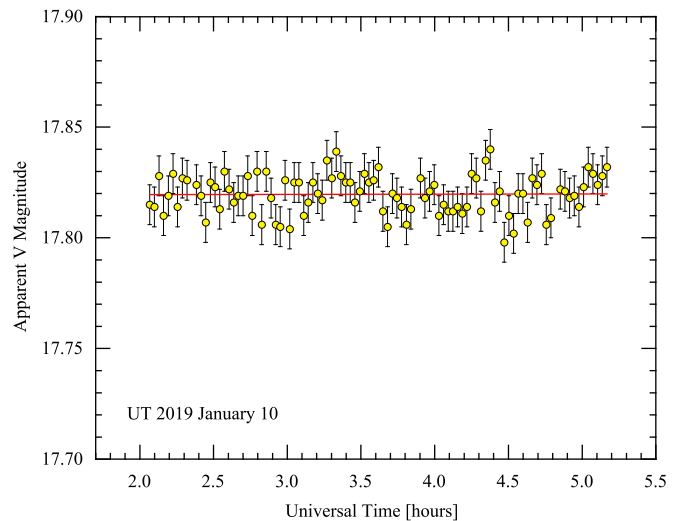
Figure 6. Light curve measured within a 20 pixel ($4\rlap{.}{''}3$) radius circular aperture with sky subtraction from a surrounding contiguous annulus extending to $8\rlap{.}{''}6$. The red line is a linear least-squares fit to the data added to guide the eye. Representative error bars of ± 0.01 mag are shown.

Table 2
Circular Aperture Color Photometry

UT Date	Radius[a]	V	H[b]	$B - V$	$V - R$	$B - R$
2019 Jan 10	4.3	17.82 ± 0.02	13.73	0.78 ± 0.03	0.40 ± 0.03	1.18 ± 0.03
2019 Feb 21	4.3	17.61 ± 0.02	14.62	0.75 ± 0.03	0.41 ± 0.03	1.16 ± 0.03
Sun[c]	...	...	...	0.64 ± 0.02	0.35 ± 0.01	1.00 ± 0.02

Notes.
[a] Angular radius of circular photometry aperture, in arcseconds.
[b] Absolute magnitude, from Equation (1). The uncertainty is dominated by the unmeasured phase function and is of order several $\times 0.1$ mag.
[c] Colors of the Sun from Holmberg et al. (2006).

Table 3
Rectangular Aperture Color Photometry[a]

Region[b]	x_{min}, x_{max}	y_{min}, y_{max}	V	$B - V$	$V - R$	$B - R$
Nucleus	-2.2, 2.2	-2.2, 2.2	17.88 ± 0.01	0.78 ± 0.01	0.40 ± 0.01	1.18 ± 0.01
Tail A	2.2, 44.9	-2.2, 2.2	20.51 ± 0.02	0.77 ± 0.08	0.42 ± 0.05	1.19 ± 0.09
Tail A	44.9, 87.9	-2.2, 2.2	20.94 ± 0.03	0.81 ± 0.10	0.52 ± 0.08	1.33 ± 0.11
Sun[c]	...	...	...	0.64 ± 0.02	0.35 ± 0.01	1.00 ± 0.02

Notes.
[a] All data from UT 2019 January 10.
[b] Rectangle defined by $x_{min} \leqslant x'' \leqslant x_{max}$, $y_{min} \leqslant y'' \leqslant y_{max}$, with the nucleus at $x'' = y'' = 0$, and x increasing along the tail to the west.
[c] Colors of the Sun from Holmberg et al. (2006).

with each tail. On Tail A we used a box extending $70''$ along the tail and $10''$ perpendicular, while for the shorter Tail B, these dimensions were $50''$ and $10''$, respectively. The sky background was determined from the clipped median signal in a series of adjacent regions. As the visible tails are longer than the measurable tails, it is clear that the results provide lower limits to the true brightness and cross section of the ejected dust. The integrated brightness of Tail A is equivalent to $V_A = 15.2 \pm 0.2$ and of Tail B, $V_B = 17.2 \pm 0.3$, where the errors reflect the difficulty of measuring low surface brightness diffuse structures against structured backgrounds. These correspond, through Equation (1), to $H_A = 12.3 \pm 0.2$ and $H_B = 14.3 \pm 0.3$ (neglecting additional uncertainties due to the unmeasured phase function). The effective cross sections (Equation (2)) are $C_A = 175 \pm 35$ km^2 and $C_B = 28 \pm 9$ km^2. Only very crude photometry of Tail C is possible, because it has extremely low surface brightness. We estimate $V_C = 19.7 \pm 0.7$, $H_C = 16.8 \pm 0.7$, and $C_C = 3 \pm 2$ km^2 from the image on UT 2019 April 10. For comparison, the geometric cross section of a 3 km radius sphere is 28 km^2.

If contained entirely in spherical particles of density, ρ, and radius, $\overline{a}$, the dust mass is given by $M_d \sim \rho \overline{a} C_e$. For example, with $\rho = 1000$ kg m^{-3}, $\overline{a} = 0.2$ mm, the implied dust masses are $M_A \sim 4 \times 10^7$ kg, $M_B \sim 6 \times 10^6$ kg, and $M_B \sim 6 \times 10^5$ kg, respectively. Taking the event lifetimes for all three tails as 10–20 days, we infer approximate mass production rates $dM_A/dt \sim 20$–40 kg s^{-1}, $dM_B/dt \sim 4$–6 kg s^{-1}, and $dM_C/dt \sim 0.4$–0.6 kg s^{-1}.

2.3. Colors

We obtained three pairs of BV measurements on UT 2019 January 10 and two pairs on UT 2019 February 21, in order to determine the optical colors of Gault. Measurements of $B - V$ and $V - R$ using circular apertures centered on the photocenter are summarized in Table 2. Essentially identical central colors

are obtained on the two dates, with mean values $B - V = 0.77 \pm 0.02$ and $V - R = 0.41 \pm 0.02$, which are redder than the Sun by 0.12 ± 0.02 and 0.06 ± 0.02 mag, respectively.

As noted above, the cross section in the data from UT 2019 January 10 is dominated by dust, while by UT 2019 February 21 the cross section is within $\sim 20\%$ of the value obtained from the JPL Horizons database (which presumably represents Gault in an inactive state). The fact that the colors remain unchanged even as the scattering cross section changes from dust-dominated to nucleus-dominated is evidence that the colors of the nucleus and the dust are similar. To directly measure the color of the dust free from contamination by the nucleus, we rotated the composite image from UT 2019 January 10 (Figure 1) to bring the tail to the horizontal, then measured the signal within projected rectangular apertures, with results summarized in Table 3. In the central or nucleus region, we obtained colors that are consistent with those from circular aperture photometry (Table 2). The colors of the dust in Tail boxes A1 and A2 are consistent with those in the central region within the uncertainties of measurement (Table 3), showing that the data provide no evidence for spatial variation of color along the tail of Gault. Tables 2 and 3 show that the color of Gault is stable with respect to time and position.

The colors of Gault are compared with those of other asteroid spectral types from Dandy et al. (2003) in Figure 7. Gault is optically too blue to be an S-type, and is closer to the less-metamorphosed members of the C-type complex. While this makes Gault slightly unusual relative to other members of the Phocaea family, 75% of which are S-types, Carvano et al. (2001) reported that 15% of Phocaea family members are C-types. Separately, Novaković et al. (2017) identified a low-albedo family within the Phocaea group that we tentatively associate with the C-types.

Table 4
Dust Model Parameters[a]

Feature	v_0[b]	t_0[c]	τ[d]	q_1[e]	q_2[f]
Tail A	0.15 ± 0.05	2018 Oct 28 $\pm$ 5	10	3.0 ± 0.1	4.2 ± 0.2
Tail B	0.15 ± 0.05	2018 Dec 31 $\pm$ 5	5	2.7 ± 0.2	4.2 ± 0.2

Notes.
[a] Results from Monte Carlo simulations.
[b] Dust ejection velocity (m s^{-1}).
[c] Tail initiation date.
[d] e-folding fading time, in days.
[e] Size distribution index for particle radii $40 \leqslant a \leqslant 120$ μm.
[f] Size distribution index for particle radii $120 \leqslant a \leqslant 5000$ μm.
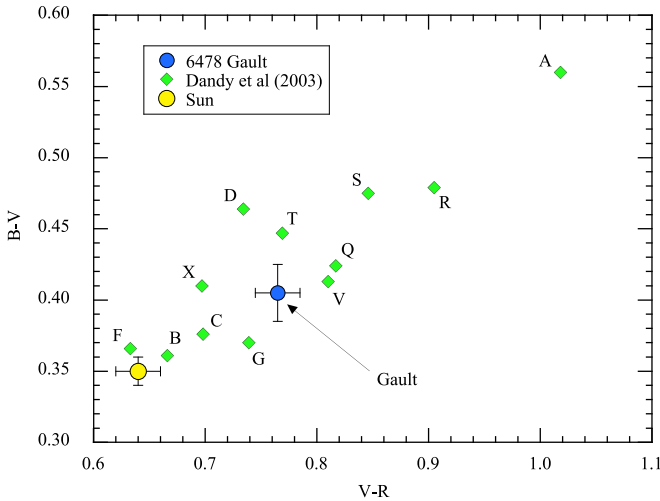
Figure 7. Color–color diagram comparing Gault (blue circle with error bars) to various asteroid spectral types from Dandy et al. (2003), (green diamonds) as marked. The color of the Sun is indicated by a yellow circle, from Holmberg et al. (2006).

2.4. Spectrum

The optical reflection spectrum of Gault was obtained on UT 2019 January 20, again at the NOT. We used a 1″ wide slit with Grism #3, which is ruled at 400 line mm^{-1} and gives a dispersion 2.3 Å pixel^{-1}. The resulting spectral resolution $\lambda/\Delta\lambda \sim 350$. Two integrations of 1200 s each were obtained, together with a 5 s integration on the $V = 7.8$ mag, G2V solar analog star HIP 53172. The asteroid and the star were observed at comparable airmasses of 1.46–1.54 (Gault) and 1.52 (star), respectively, in order to cancel both telluric and solar spectral features. The atmospheric seeing was 0″8–0″9, FWHM.

We extracted the spectrum using a 4″3 wide region centered on the peak brightness of the continuum. After flattening the data using a near-simultaneous spectrum of a quartz lamp, and wavelength calibration using emission lines from an internal HeNe source, the comet and solar analog spectra were divided to produce a reflectivity spectrum. Finally, we removed the slope of the spectrum using a least-squares fit, and normalized the result to unity at $\lambda = 5500$ Å (Figure 8). We calibrated the continuum using the measured V-band (central wavelength $\lambda_c = 5500$ Å) magnitude, $V = 17.82$, and the fact that a $V = 0$ star has flux density $f_\lambda = 3.75 \times 10^{-9}$ erg cm^{-2} s^{-1} Å^{-1} (Drilling & Landolt 2000). We estimate that the mean V-band continuum flux density of Gault is $f_V = 2.8 \times 10^{-16}$ erg cm^{-2} s^{-1} Å^{-1}.
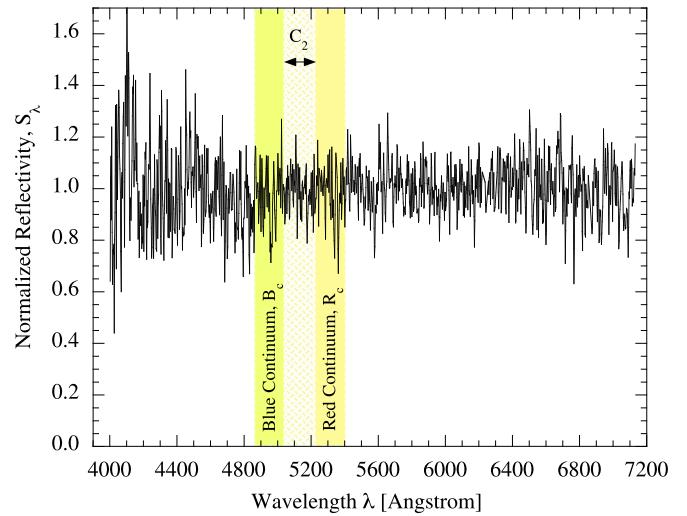

Figure 8. De-sloped reflectivity spectrum normalized to unity at $\lambda = 5500$ Å, from UT 2019 January 20. Vertical bands show the wavelengths of the C_2 band and flanking blue and red continua (B_c and R_c, respectively) used to estimate the noise.

Active comets exhibit several emission bands due to resonance fluorescence in cometary gas. The strongest bands in the optical are from OH (3080 Å) and CN (3883 Å), neither of which fall within the sensitive range of the NOT spectrograph. The strongest band in the 4000–7000 Å range is from $C_2 \Delta V = 0$, which is largely confined to the range of wavelengths 5050 Å $\leqslant \lambda \leqslant 5220$ Å (see Farnham et al. 2000). The spectrum of Gault shows no evidence for emission bands at any wavelength. We define adjacent continuum windows of equal width both blueward (4880 Å $\leqslant \lambda \leqslant 5049$ Å, called "B_C") and redward (5221 Å $\leqslant \lambda \leqslant 5390$ Å, "R_C") of the C_2 band in order to assess the noise on the data. These wavelength bands are indicated in Figure 8. Expressed as a fraction of the continuum, the statistical uncertainties are found to be ± 0.013, ± 0.010, and ± 0.013 in the B_C, $C_2 \Delta V$, and R_C bands, respectively. We take the largest of these values, namely $1\sigma = 0.013$, as the best estimate of the fractional uncertainty on the continuum in the $C_2 \Delta V$-band. Then, 3σ corresponds to a flux density $f_{C2} = 0.039 f_V = 6.5 \times 10^{-18}$ erg cm^{-2} s^{-1} Å^{-1} (where we have included a correction of 0.6 for slit losses) and this is our empirical upper limit to the gas flux density. Over the $\Delta\lambda = 170$ Å width of the $C_2 \Delta V$-band, the 3σ limit to the flux is $F = f_{C2}\Delta\lambda \leqslant 1.1 \times 10^{-15}$ (erg cm^{-2} s^{-1}).

Provided that the coma is optically thin, the number of C_2 molecules projected within the slit, N, is directly proportional to F, following

$$N = \frac{4\pi\Delta^2 F}{g(r_H)}. \quad (3)$$

Here, $g(r_H)$ is the fluorescence efficiency factor of the $C_2 \Delta V = 0$ band at heliocentric distance r_H au. We take $g(1) = 2.2 \times 10^{-13}$ erg s^{-1} radical^{-1} (A'Hearn 1982) and scale to the heliocentric distance of Gault by the inverse square law, finding $g(2.446) = 3.7 \times 10^{-14}$ erg s^{-1} radical^{-1}. Substituting into Equation (3) gives $N \leqslant 4 \times 10^{26}$ as the 3σ upper limit to the number of C_2 radicals in the projected $1″0 \times 4″3$ slit.
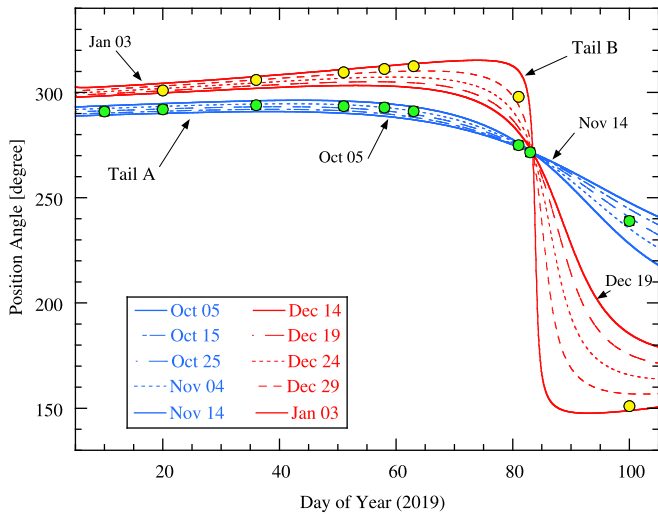
Figure 9. PAs of Tails A and B measured as a function of time, expressed as day-of-year (DOY = 1 corresponds to UT 2019 January 1). The overplotted lines show synchrones for different ejection dates. We show five synchrones for each tail, with a spacing of 10 days for Tail A in the range UT 2018 October 15 to November 9, and 5 days for Tail B in the range UT 2018 December 19 to 2019 January 3. Error bars are smaller than the plot symbols.

To scale from N to the production rate of C_2 we need a model to estimate the fraction of the C_2 coma captured within the projected slit. Following cometary tradition, and while recognizing the flaws and uncertainties of the procedure, we use the Haser model formalism, in which the distribution of the radical is assumed to be described by two exponentials with scale lengths characterizing the "parent" and the "daughter" species. We use scale lengths at $r_H = 1$ au of $L_P = 2.5 \times 10^4$ km and $L_D = 1.2 \times 10^5$ km (Cochran 1985), and scale to the heliocentric distance of Gault using $L_{P,D}(r_H) = L_{P,D}(1)r_H^2$. The speed of outflowing gas molecules, needed to estimate the residence time in the projected slit, was taken to be 0.5 km s^{-1}.

Finally, we find that the non-detection of the C_2 $\Delta V = 0$ band corresponds to a production rate $Q_{C2} \leqslant 1 \times 10^{23}$ s^{-1}. In comets, the median ratio of C_2 to hydroxyl production rates is $C_2/OH = 10^{-2.5}$, albeit with a tail extending to values as low as 10^{-4} (A'Hearn et al. 1995). The median value would give a spectroscopic limit on the OH production rate limit $Q_{OH} \leqslant 3 \times 10^{25}$ s^{-1} and mass loss rates in water of $dM/dt \leqslant 1$ kg s^{-1}. This limit is comparable to values set spectroscopically on active asteroids (e.g., Jewitt 2012), smaller than the dust production rates inferred in Section 2.2, and 10^2 to 10^3 times smaller than commonly measured in short-period comets. At $r_H = 2.446$ au, a perfectly absorbing water-ice surface oriented perpendicular to the Sun–Gault line would sublimate in thermodynamic equilibrium at the specific rate $f_s = 5.6 \times 10^{-5}$ kg m^{-2} s^{-1}. The empirical spectroscopic limit then sets a limit to the area of exposed ice f_s^{-1} $dM/dt \leqslant$ 18,000 m^2 (0.02 km^2).

3. Discussion

3.1. Dust Properties

The PAs of the tails (Table 1) are plotted as functions of time in Figure 9. Lines in the figure show the PAs of synchrones computed for a range of dates for each tail. For Tail A, the synchrones span the period UT 2018 October 5 to November 14, with an interval of 10 days. For Tail B, the synchrones span

UT 2018 December 19 to 2019 January 3, with an interval of 5 days. Evidently, the PAs of the Gault tails are inconsistent with any single isochrone, but compatible with isochrones for dust emitted over discrete ranges of dates. The middle times for the isochrone models of Tails A and B are UT 2018 October 30 and UT 2018 December 28, respectively, each with an uncertainty of a few days. Results for Tail C (not plotted in Figure 9) are less certain, both because the tail is very faint and difficult to measure and because we so far possess only one measurement from UT 2019 April 10. Our best estimate of the initiation date is UT 2019 February 10 ± 7.

These results imply that Tail A was ~72 days old when imaged on UT 2019 January 10 (Figure 1) while Tail B was ~23 days old when first recorded in the image from UT 2019 January 20 (inset to Figure 1). Tail A extends to the edge of the field of view in Figure 1, an angular distance of 250″. At geocentric distance $\Delta = 1.83$ au (Table 1) this corresponds to a linear distance $\ell = 3.3 \times 10^8$ m in the plane of the sky. Particles released from the nucleus with zero initial velocity and accelerated thereafter by radiation pressure would travel a distance $\ell = \beta g_\odot(1) (\Delta t)^2/(2r_H^2)$, where r_H is the heliocentric distance expressed in astronomical units and $g_\odot(1) = 0.006$ m s^{-2} is the gravitational acceleration to the Sun at $r_H = 1$ au. Δt is the time since ejection; we set $\Delta t = 72$ days $(6.2 \times 10^6$ s). Dimensionless quantity β is the ratio of the acceleration due to radiation pressure to the acceleration due to solar gravity, and is a function of the particle shape, porosity, density, and composition but, most importantly, of size (Bohren & Huffman 1983). These parameters are unknown for Gault. For convenience, we assume that $\beta = 10^{-6}/a$, with a in meters, which is true for grains of density $\rho = 570$ kg m^{-3}. Substituting, we find $\beta = 0.02$, corresponding to $a \sim 50\,\mu$m. Because the tail is unlikely to lie in the plane of the sky, ℓ must be considered a lower limit to the true length, and so $\beta \gtrsim 0.02$ and $a \lesssim 50\,\mu$m. (For example, on UT 2019 January 10, the phase angle was $\alpha = 20°$ (Table 1). If the tail were aligned with the antisolar direction, the actual length would be larger than the plane-of-sky length by a factor $1/\sin(\alpha) \sim 3$, giving β three times larger and a three times smaller than our nominal estimate). Larger particles lurk closer to the nucleus. For example, 25″ down the tail the particle size suggested by radiation pressure acceleration is $a \sim 500\,\mu$m. The same argument applied to Tail B, which has plane-of-sky length ~15″ on UT 2019 January 20 (Figure 1), gives $\ell \gtrsim 2.0 \times 10^7$ m and $\beta \gtrsim 0.1$, and $a \lesssim 10\,\mu$m. These order of magnitude considerations indicate that the particles ejected from Gault are all very large compared to the wavelength of light. We estimate a mean particle radius in Tail A $\bar{a} \sim 100\,\mu$m.

Figure 4 shows Gault on UT 2019 March 24, from a perspective only $\delta_E = 0°26$ above the orbital plane. With this viewing geometry, the effects of projection are minimized, although not eliminated, and we obtain a measure of the extent of the dust tail that is perpendicular to the plane of the orbit. Notice that Tails A and B appear merged, indicating that they both lie close to the orbital plane of Gault. To measure the FWHM, $\theta_{1/2}$, we rotated the image to bring the dust tail to the horizontal and then made a series of vertical cuts across the tail, each 100 pixel (21″5) wide. The results are shown in Figure 10. The width increases slowly with distance from the nucleus. At its narrowest, ~25,000 km from the nucleus, we find $\theta_{1/2} = 2″9 \pm 0″3$, corresponding to 3000 ± 300 km. The tail is broad compared to the $\theta = 1″0$ FWHM seeing in the
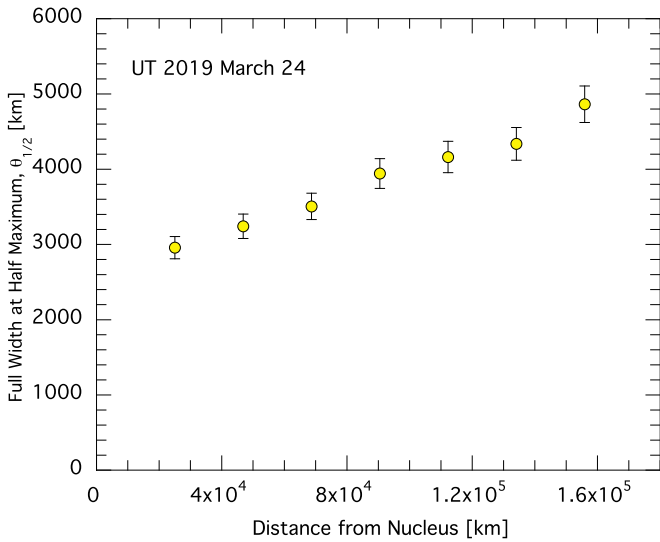
Figure 10. FWHM, $\theta_{1/2}$, of the tail measured on UT 2019 March 24 from a position 0°.26 above the orbital plane of Gault.

Figure 4 image composite, indicating that it is fully resolved. To test this, we also measured the higher resolution *HST* data taken UT 2019 March 22 from a larger angle ($\delta_E = 0°.7$, Table 1) finding a similar width ($\theta_{1/2} = 2''.8 \pm 0''.3$).

We use $\theta_{1/2}$ to make a simple estimate of the dust ejection velocity from Gault. Given that this location samples primarily Tail A, which was ejected on UT 2018 October 28, we infer that the dust age is $\Delta t = 1.2 \times 10^7$ s. The half-width then gives an estimate of the ejection speed perpendicular to the orbit as $V_\perp = \theta_{1/2}/(2\Delta t)$. Substituting, we find $V_\perp = 0.13 \pm 0.01$ m s^{-1}. This is an upper limit to the speed because the measured width in Figure 10 is potentially still affected by projection, even though the out-of-plane angle is only 0°.26. The escape speed from a non-rotating 3 km radius sphere of density $\rho = 10^3$ kg m^{-3} is $V_e \sim 2$ m s^{-1}. Escape with $V_\perp < V_e$ is consistent with rotation near breakup.

We separately used a Monte Carlo model (developed by Ishiguro et al. 2007) to estimate the dust properties. The advantage of the model is that it allows the influence of specific assumed dust parameters to be systematically explored. The disadvantage is that the number of relevant parameters is very large and the model is under-constrained by the data. We proceeded to adjust the model iteratively in order to test the sensitivity of the tail morphology to different dust and ejection parameters.

The motion of ejected particles is affected by their initial velocity, v_0, by their direction of ejection, and by the magnitude of radiation pressure factor β. The gross morphology of the tail is also influenced by the time profile of the emission. Inspection of the rising portions of the maxima in Figure 2 of Ye et al. (2019) shows that dust emission continued over 10–20 days for both Tails A and B. We parameterized the emission for each tail as an exponential, $dM/dt \propto \exp(-(t - t_0)/\tau)$, where t_0 is the initiation time and τ is the e-folding time. We assumed that the velocity versus radius relation is of the form $v(a) = v_0 a^{-\gamma}$, with γ constant, and we tested two values; $\gamma = 1/2$ describes particle acceleration against gravity by gas drag, while $\gamma = 0$ describes size-independent ejection, as might be expected from rotational breakup. We could not find agreeable solutions using $\gamma = 1/2$ and, further motivated by the very slight measured flaring of the dust tail when viewed edgewise (Figure 10),
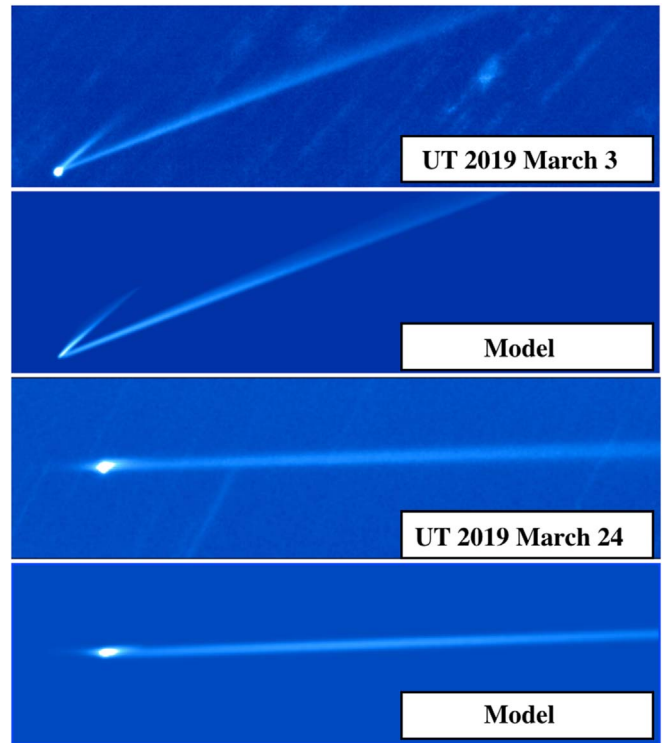

Figure 11. Data and simulations of Gault for (top two panels) UT 2019 March 3 and (bottom two panels) March 24, using the parameters listed in Table 4.

adopted $\gamma = 0$ for all models. It is conventional to assume that the particles are distributed in size such that the number of particles with radius in the range a to $a + da$ is $n(a)\, da = \Gamma a^{-q}\, da$, where Γ and q are constants. However, we found that acceptable fits to the data could not be obtained using this single power-law relation, regardless of the choice of q. Instead, we introduced a double power law to better fit the data.

For both tails A and B (Table 4), we found acceptable solutions for $v_0 = 0.15 \pm 0.05$ m s^{-1}, which is in excellent agreement with our estimate (0.13 ± 0.01 m s^{-1}) based on analysis of the plane-crossing data. For Tail A, ejection started on $t_0 =$ UT 2018 October 28 and had an e-folding time $\tau_A = 10$ days. For Tail B we found $t_0 =$ UT 2018 December 31 and fading time $\tau_B \sim 5$ days. For both tails, the size distribution in the range $40 \leqslant a \leqslant 120\,\mu$m has $q = 3.0 \pm 0.3$, while for $120 \leqslant a \leqslant 5000\,\mu$m we find a steeper $q = 4.2 \pm 0.2$. The overall similarity of the solutions suggests that the same physical process is responsible for the loss of material in Tails A and B. The cross-section weighted mean particle radius in this distribution is $\bar{a} = 210\,\mu$m, with an uncertainty that is at least a factor of two. We note that these parameters are broadly consistent with the isochrones in Figure 9. Initiation times for Tail A, UT 2018 October 18 ± 5, and Tail B, UT 2018 December 24 ± 1, deduced photometrically (Ye et al. 2019) are both slightly earlier than deduced from the dust tail model. The resulting image-plane models are shown in Figure 11.

The size distribution found by Ye et al. (2019) is qualitatively similar to that found here, with $q = 3.0$ for $10 \leqslant a \leqslant 20\,\mu$m and $q = 4.0$ for larger particles. Moreno et al. (2019) reported three power-law segments with indices $q = 2.28$ ($1 \leqslant a \leqslant 15\,\mu$m), 3.95 ($15 \leqslant a \leqslant 870\,\mu$m), and 4.22 ($a > 870\,\mu$m) and employed a $v \propto a^{-\gamma}$ relation with $\gamma = 1/2$, as appropriate for gas drag ejection (although they considered the presence of ice to be unlikely, as do we). A
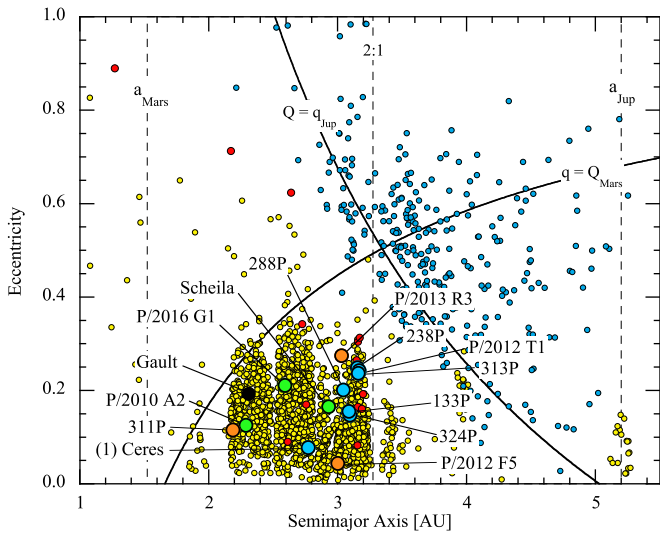
Figure 12. Semimajor axis vs. orbital eccentricity for main-belt asteroids (small yellow circles), comets (small blue circles), and active asteroids. The latter are color coded by their suspected physical origin; ice sublimation (filled blue circles), impact debris (filled green circles), rotational breakups (filled orange circles), and other, mostly unknown origins (filled red circles). Gault is indicated by a filled black circle. Diagonal arcs show the loci of orbits having perihelion distances equal to the aphelion distance of Mars, and aphelion distances equal to the perihelion distance of Jupiter, as marked. Vertical dashed lines indicate the semimajor axes of Mars, Jupiter, and the 2:1 mean-motion resonance with Jupiter. Some active asteroids whose symbols overlap at the scale of the plot have been slightly displaced for clarity.

significantly flatter power-law index, $q \sim 1.6$, was reported by Kleyna et al. (2019). However, the latter assumed a single power-law distribution from 10 to $10^3 \, \mu m$ and did not specify their choice of γ. The models are broadly consistent in their identification of dominantly large particles ejected at speeds comparable to or less than the escape speed from Gault.

3.2. Origin of the Activity

The active asteroid closest in semimajor axis to Gault is 354P/(2010 A2; see Figure 12), the photometric and morphological properties of which are all indicative of asteroid–asteroid impact (Jewitt et al. 2010, 2013b, Kim et al. 2017a, 2017b). Other examples of likely impact-produced active asteroids are shown in Figure 12 as green-filled circles. However, we reject impact as a likely cause of mass loss in Gault for two reasons. First, both the PA data (Figure 9) and the photometry (Ye et al. 2019) indicate non-impulsive emission occurring over intervals of ∼10–20 days, whereas impact should be impulsive. Second, the existence of three widely spaced tails cannot be reconciled with a single impact in any but the most contrived way, and the probability of three consecutive impacts is negligible.

Several examples of ice-sublimating active asteroids are known. However, these differ from Gault by ejecting dust smoothly near perihelion (true anomalies $\nu \sim 0° \pm 90°$; see Hsieh et al. 2018) and do not show the discrete emission required to explain Tails A and B. Specifically, it is not obvious why exposed ice would sublimate in fortnight-long windows separated by intervals of months, and Gault is far from perihelion, with true anomaly 240°–260° (Table 1). In addition, the isothermal blackbody temperature in Gault's inner-belt orbit is 180 K, reducing (but, admittedly, not eliminating) the prospects that water ice could survive. Indeed, the best-
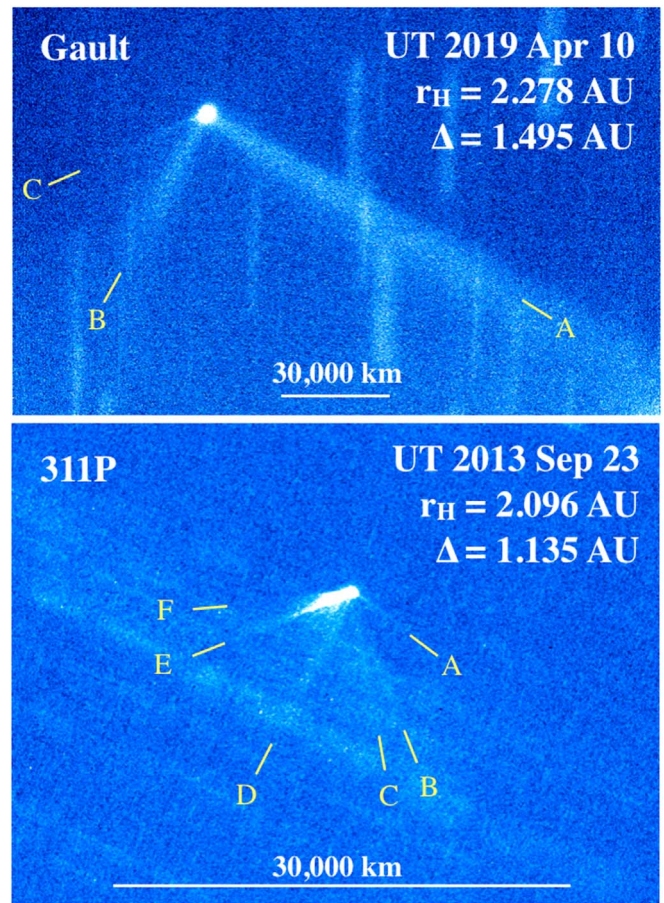
Figure 13. Active asteroids Gault (top panel) and 311P (bottom panel, from Jewitt et al. 2013a) compared. Discrete tails of the two bodies are labeled and a 30,000 km scale bar is shown in each panel. Gault is physically much larger and brighter than 311P but shares a common appearance, consisting of separate tails coinciding with individual pulses of mass loss, each characterized by a different synchrone. Both panels have north to the top and east to the left.

established ice sublimators are located in the outer belt (filled blue circles in Figure 12), where temperatures are lower. For these reasons we reject ice sublimation as a likely cause of activity in Gault. We also note that the spectra show no evidence for gas (Figure 8), although our data are insensitive to emissions from the likely mass-dominant volatile H_2O.

The active asteroid second closest in semimajor axis to Gault in Figure 12 is 311P/(2013 P5). Figure 13 shows a comparison between these two objects. Object 311P ejected dust impulsively and aperiodically, producing nine separate tails spread over 9 months (Jewitt et al. 2013a, 2015, 2018), with about 10^5 kg of dust per ejection. In between ejections, the nucleus of 311P appears to have been inactive, which is consistent with the interpretation that each tail formation event signifies the loss of surface fines following local instabilities ("landslides") on a critically rotating body (Jewitt et al. 2013a, Hirabayashi et al. 2015). Although Gault (so far) has only three tails, the morphological similarity to 311P is striking, leading us to suspect that Tails A, B, and C are products of incipient rotational instability on a rapidly rotating nucleus. One potentially important difference is that 311P is very small, with an estimated radius ∼190 ± 30 m (Jewitt et al. 2018), whereas Gault is ∼15 times larger (and ∼3500 times more massive), with equivalent circular radius ∼2.9 km (from Equation (2) with $H = 14.4$ and $p_V = 0.1$). Assuming that

9

neither body contains ice, the torque needed to accelerate the spin presumably comes from solar photons and the Yarkovsky–O'Keefe–Radzievskii–Paddack (YORP) effect. The YORP spin-up timescale, all else being equal, is proportional to radius^2. Gault would take $15^2 \sim 225$ times longer to reach critical spin than would 311P. The YORP time for 311P is only ~ 0.1 Myr (Jewitt et al. 2018), corresponding to 22 Myr when scaled to the size of asteroid Gault. This longer timescale is still short compared to the collisional destruction timescale, which for a 3 km radius main-belt body is $\sim 10^9$ yr (Bottke et al. 2005). We conclude that YORP spin-up is capable of driving Gault to incipient rotational instability.

It is interesting to consider the relative amounts of material shed by 311P and Gault. A tail mass M, if spread uniformly over the parent body of radius r_n, would have a thickness, d, given by $d = M/(4\pi\rho r_n^2)$. Substituting, for M_A and M_B, we find $d_A = 0.4$ mm and $d_B = 0.06$ mm, respectively. For comparison, on 311P (with $r_n = 0.29$ km; Jewitt et al. 2018) the 10^5 kg ejected per event corresponds to $d \sim 0.2$ mm, which is surprisingly similar to the Gault value. In other words, the ejected mass scales roughly as r_n^2, as might be expected for a surface instability. The reason behind the long duration of mass loss in Gault (e-folding timescales of 5–10 days) is less clear. Our naive expectation is that mass would fall off the surface on the freefall timescale $(G\rho)^{-1/2} \sim$ hours, rather than days, as observed. Numerical simulations perhaps provide a hint by showing that, contrary to intuition, unstable systems can survive for days and even years before collisional dissipation and secondary spin fission can lead to the final state (e.g., Boldrin et al. 2016).

Sadly, photometry to date provides no convincing evidence concerning rotation, presumably in part because of the diluting effects of near-nucleus dust. However, a test for rotational instability should become possible through the acquisition of a rotational light curve once the near-nucleus dust has cleared. If the hypothesis is correct, we should find that Gault is rotating near the ~ 0.1 day critical period for instability (e.g., Pravec et al. 2008). It will probably have a very small light curve amplitude, as a result of the "muffin-top" morphology observed by radar and by direct imaging in several asteroids likely to have been shaped by rotational losses. The identification of additional discrete tails, either in prediscovery data or in observations yet to be made, or both, would further strengthen the resemblance to the nine-tailed 311P.

4. Summary

We present initial observations of active asteroid 6478 Gault. We argue that Gault is an analog of the rotationally unstable asteroid 311P/(2013 P5), in which multiple tails result from episodes of equatorward avalanching, followed by pick-up of the debris by solar radiation pressure. Specific observations include the following.

1. 6478 Gault emitted dust with optical colors more C-like than S-like, in three distinct events. The first ejection began on UT 2018 October 28 ± 5, the second on UT 2018 December 31 ± 5, and the third on UT 2019 February 10 ± 7, with durations 10–20 days, and no measurable emission in between.

2. The dust particles follow a broken power-law size distribution, with index $q = 3.0 \pm 0.3$ for $40 \leqslant a \leqslant 120 \,\mu$m and $q = 4.2 \pm 0.2$ for $120 < a \leqslant 5000 \,\mu$m. The cross-section weighted mean radius is $\bar{a} = 0.2$ mm. We infer dust masses $M_A \sim 4 \times 10^7$ kg, $M_B \sim 6 \times 10^6$ kg, and $M_C \sim 6 \times 10^5$ kg. The dust was ejected slowly, with speeds ~ 0.15 m s^{-1} and we find average mass loss rates $dM_A/dt \sim 20$–40 kg s^{-1}, $dM_B/dt \sim 4$–6 kg s^{-1}, and $dM_C/dt \sim 0.4$–0.6 kg s^{-1}.

3. We set an upper limit to the production of C_2 molecules at $Q_{C2} \leqslant 1 \times 10^{23}$ s^{-1}. Given a nominal cometary ratio $C_2/\text{OH} = 10^{-2.5}$, the inferred upper limit to the production rate of water is $\leqslant 1$ kg s^{-1}, corresponding to an upper limit to the area of exposed water ice < 0.02 km^2.

4. Despite the likelihood that rotational instabilities drive the current mass loss, time-series photometry of the nucleus region shows no evidence for rotational or other modulation.

ORCID iDs

Ralf Kotulla ⓘ https://orcid.org/0000-0002-4460-9892

References

A'hearn, M. F. 1982, in Comets, ed. L. L. Wilkening (Tucson, AZ: Univ. Arizona Press), 433
A'Hearn, M. F., Millis, R. C., Schleicher, D. O., Osip, D. J., & Birch, P. V. 1995, Icar, 118, 223
Blanton, M. R., Bershady, M. A., Abolfathi, B., et al. 2017, AJ, 154, 28
Bohren, C. F., & Huffman, D. R. 1983, Absorption and Scattering of Light by Small Particles (New York, Chichester, Brisbane, Toronto, Singapore: Wiley)
Boldrin, L. A. G., Scheeres, D. J., & Winter, O. C. 2016, MNRAS, 461, 3982
Bottke, W. F., Durda, D. D., Nesvorný, D., et al. 2005, Icar, 179, 63
Carvano, J., Lazzaro, D., Mothe-Diniz, T., et al. 2001, Icar, 149, 173
Cochran, A. L. 1985, AJ, 90, 2609
Dandy, C. L., Fitzsimmons, A., & Collander-Brown, S. J. 2003, Icar, 163, 363
Drilling, J. S., & Landolt, A. U. 2000, in Allen's Astrophysical Quantities, ed. N. C. Arthur (4th ed.; New York: AIP, Springer), 381
Farnham, T. L., Schleicher, D. G., & A'Hearn, M. F. 2000, Icar, 147, 180
Hainaut, O. R., Boehnhardt, H., Snodgrass, C., et al. 2014, A&A, 563, A75
Harbeck, D. R., Boroson, T., Lesser, M., et al. 2014, Proc. SPIE, 9147, 91470P
Hirabayashi, M., Sánchez, D. P., & Scheeres, D. J. 2015, ApJ, 808, 63
Holmberg, J., Flynn, C., & Portinari, L. 2006, MNRAS, 367, 449
Hsieh, H. H., Ishiguro, M., Kim, Y., et al. 2018, AJ, 156, 223
Hsieh, H. H., & Jewitt, D. 2006, Sci, 312, 561
Ishiguro, M., Sarugaku, Y., Ueno, M., et al. 2007, Icar, 189, 169
Jewitt, D. 2012, AJ, 143, 66
Jewitt, D., Agarwal, J., Weaver, H., Mutchler, M., & Larson, S. 2013a, ApJL, 778, L21
Jewitt, D., Agarwal, J., Weaver, H., Mutchler, M., & Larson, S. 2015, ApJ, 798, 109
Jewitt, D., Ishiguro, M., & Agarwal, J. 2013b, ApJL, 764, L5
Jewitt, D., Weaver, H., Agarwal, J., Mutchler, M., & Drahus, M. 2010, Natur, 467, 817
Jewitt, D., Weaver, H., Mutchler, M., et al. 2018, AJ, 155, 231
Kim, Y., Ishiguro, M., & Lee, M. G. 2017a, ApJL, 842, L23

Kim, Y., Ishiguro, M., Michikami, T., & Nakamura, A. M. 2017b, AJ, 153, 228

Kleyna, J. T., Hainaut, O. R., Meech, K. J., et al. 2019, ApJL, 874, L20

Kotulla, R. 2014, adass XXIII, 485, 375

Landolt, A. U. 1992, AJ, 104, 340

Moreno, F., Licandro, J., Jehin, E., et al. 2019, arXiv:1903.09943

Novaković, B., Tsirvoulis, G., Granvik, M., & Todović, A. 2017, AJ, 153, 266

Pravec, P., Harris, A. W., Vokrouhlický, D., et al. 2008, Icar, 197, 497

Smith, K. W., Denneau, L., Vincent, J.-B., & Weryk, R. 2019, CBET, 4594, 1

Ye, Q., Kelley, M. S. P., Bodewits, D., et al. 2019, ApJL, 874, L16